# Experiments and Simulations of n-Heptane Spray Auto-Ignition in a Closed Combustion Chamber at Diesel Engine Conditions



**Author(s):**
Wright, Yuri Martin; Margari, Ourania-Nektaria; Boulouchos, Konstantinos; Paola, Giorgio de; Mastorakos, Epaminondas

**Publication date:**
2010

**Permanent link:**
https://doi.org/10.3929/ethz-b-000017481



**Originally published in:**
Flow, Turbulence and Combustion 84(1), https://doi.org/10.1007/s10494-009-9224-0

Flow Turbulence Combust (2010) 84:49–78
DOI 10.1007/s10494-009-9224-0

# Experiments and Simulations of *n*-Heptane Spray Auto-Ignition in a Closed Combustion Chamber at Diesel Engine Conditions

**Yuri M. Wright · Ourania-Nektaria Margari · Konstantinos Boulouchos · Giorgio De Paola · Epaminondas Mastorakos**

Received: 11 July 2008 / Accepted: 11 May 2009 / Published online: 30 May 2009


**Abstract** Auto-igniting *n*-heptane sprays have been studied experimentally in a high pressure, high temperature constant volume combustion chamber with optical access. Ignition delay and the total pressure increase due to combustion are highly

Y. M. Wright (✉)
Aerothermochemistry and Combustion Systems Laboratory, ETH Zurich,
ML L16, CH-8092, Zürich, Switzerland
e-mail: wright@lav.mavt.ethz.ch
URL: http://www.lav.ethz.ch

O.-N. Margari
Aerothermochemistry and Combustion Systems Laboratory, ETH Zurich,
ML L18, CH-8092, Zürich, Switzerland
e-mail: margari@lav.mavt.ethz.ch
URL: http://www.lav.ethz.ch

K. Boulouchos
Aerothermochemistry and Combustion Systems Laboratory, ETH Zurich,
ML J39, CH-8092, Zürich, Switzerland
e-mail: boulouchos@lav.mavt.ethz.ch
URL: http://www.lav.ethz.ch

G. De Paola · E. Mastorakos
Hopkinson Laboratory, Engineering Department, University of Cambridge,
Cambridge, CB1 2PZ, England

G. De Paola
e-mail: gd257@cam.ac.uk
URL: http://www.eng.cam.ac.uk

E. Mastorakos
e-mail: em257@cam.ac.uk
URL: http://www.eng.cam.ac.uk

*Present Address:*
O.-N. Margari
Alstom Power Systems, Brown Boveristrasse 7, CH-5401, Baden, Switzerland
e-mail: ourania-nektaria.margari@power.alstom.com

repeatable whereas the ignition location shows substantial fluctuations. Simulations have subsequently been performed by means of a first-order fully elliptic Conditional Moment Closure (CMC) code. Overall, the simulations are in good agreement with the experiment in terms of spray evolution, ignition delay and the pressure development. The sensitivity of the predictions with respect to the measured initial conditions, the spray modelling options as well as the chemical mechanism employed have been analysed. Strong sensitivity on the chemical mechanism and to the initial temperature on the predicted ignition delay is reported. The primary atomisation model did not affect strongly the predicted auto-ignition time, but a strong influence was found on the ignition location prediction.

**Keywords** Spray · Turbulent combustion · Auto-ignition · Experiments · Modelling · CMC

## 1 Introduction

The investigation of spray combustion at diesel engine relevant conditions poses significant difficulties both in terms of obtaining experimental data as well as with respect to accurate predictions by means of simulation. In the present study, auto-igniting sprays of *n*-heptane have been investigated experimentally in order to provide validation data for subsequent simulations by means of an elliptic, first order conditional moment closure (CMC) code.

A number of investigations are reported in the literature using optically accessible engines or similar, motored arrangements to study mixture formation or ignition and combustion of liquid fuel sprays, e.g. [1–4]. Due to the reciprocating nature of piston engines, boundary conditions as well as species, temperature and velocity fields at the time of injection exhibit a dependence on the individual realisation of the intake and compression stroke. In addition, optical access is often limited or involves significant modifications to the engine. In an effort to better define boundary and initial conditions, various test rig concepts allowing for detailed investigations and offering improved optical access are in use today to reproducibly generate environments as they are typical of diesel engines at the time of fuel injection. In some cases, the combustor vessel consists of an open, flow-through system, e.g. [5, 6], where pressurised air is electrically pre-heated. In [7], a shock tube was employed to study auto-igniting *n*-octane sprays, reporting a statistical analysis of the induction period and the spatial distribution of the ignition location. While flow-through arrangements allow for fast repetition rates, the open nature of the system implies a constant pressure environment. Hence in combusting conditions, no pressure rise can be recorded that can be used to validate the heat release following ignition and flame establishment. Other experimental apparatuses therefore employ closed chambers where such data can be acquired. These include Rapid Compression Machines (RCM) [8–10] where following a compression stroke the piston position is fixed and constant volume vessels [11–13]. For the latter, great care has to be taken during the scavenging of the chamber to avoid significant cooling of the pre-heated, pre-pressurised air due to wall heat losses. In some cases, pre-combustion is employed to attain the desired temperatures and pressures in the gas phase prior to carrying out the actual investigation. While this allows for very high pressures and temperatures,

the products of the pre-combustion process add additional uncertainties to the process of interest.

Due to the individual limitations of each of the experimental set-ups outlined above, investigations reporting jointly the variability of both ignition delay and ignition location as well as, in particular, the pressure evolution following auto-ignition of *n*-heptane sprays at diesel engine conditions are rare. The main objectives of this experiment are hence to collect such a complete data-set for subsequent simulation validation purposes. The present study therefore employs a closed combustion vessel with heated walls enabling part load diesel engine conditions without any pre-combustion. The optical accessibility of the chamber allows for Schlieren, Mie scattering, and chemiluminescence imaging data collection. While the former two optical measurement techniques enable qualitative visualisation of the gas and liquid phase spray penetrations, the latter serves as an indicator for the ignition location and the variability thereof. Each of the methods employed is well established, their combined use however allows for assessing the quality of the simulation results with regard to the spray model influence on fuel spread on the one hand and the prediction not only of the time but also the location(s) of ignition.

A number of different approaches with varying degrees of complexity are documented in the literature to numerically tackle spray and engine combustion. The correct treatment of the highly complex spray ignition process requires adequately detailed chemistry and the strong interaction of chemistry with turbulence calls for sophisticated models and precludes strong simplifications—e.g. characteristic time-scales [14]—for such systems. Hence more sophisticated approaches have been proposed including flamelet models [15–17] or flame surface density based modelling [18]. At more homogeneous conditions, e.g. in HCCI engine combustion, transported PDF approaches have also been reported in [19] which exploit in-situ tabulation of the chemistry to speed up the calculations. Other approaches utilising tabulated chemistry have been proposed for diesel spray auto-ignition in [20] and for partially premixed auto-igniting *n*-heptane flames in [21].

The simulation of non-premixed systems by means of CMC has seen successful application to turbulent piloted, lifted jet, bluff-body, swirl-stabilised and counter-flow flames [22–28] as well as auto-ignition of gaseous jets [29–31]. Concerning auto-igniting liquid fuel sprays at diesel engine relevant conditions, investigations by means of CMC have been documented in [32] for the set-up of [5] containing spray penetration and ignition delay data of *n*-heptane sprays at various temperatures. In [33], the influence of background air turbulence was further investigated for the same experimental data and the importance of the conditional transport terms during all three phases of spray combustion were demonstrated. The first demonstration to engines of an elliptic CMC code which is fully coupled to a CFD solver has been presented in [34]. The formulation allows for dynamic adjustment of the grid to the changing engine geometry and good agreement was shown for experimental pressure traces from [35] at two operating conditions. As no optical data for validation is available for these engine experiments, the main objective of the numerical part of this study is to validate the predictive capability of the CMC code with respect to the measured quantities of the experimental data from the high pressure high temperature rig. It further seeks to assess the sensitivity of the predictions with respect to small changes in initial and boundary conditions and thereby to identify the influence of uncertainties in the experimental data most commonly available as

input for simulation purposes in engines. In particular the initial temperature and pressure have been varied and two approximations for the injection rate analysed. As 'standard' spray modelling practise has been followed on the CFD solver side, the influence of the atomisation model and spray cone angle are also assessed. Furthermore, a comparison of two chemical mechanisms for *n*-heptane is presented.

This paper is structured as follows: First an overview of the experimental set-up and configuration is given followed by a description of the numerical methodology. The results from both investigations are subsequently jointly presented by first showing the experimental data, and then the numerical predictions along with the sensitivity analysis, followed by the conclusions.

## 2 Experimental Configuration

### 2.1 Combustion chamber

The experimental apparatus consists of an optically accessible, closed combustion chamber which can be filled with pre-heated gases at temperatures up to 800 K and pressures of up to 80 bars prior to injection. Following combustion, the cell can withstand peak pressures up to 250 bars. Figure 1 shows an overview of the complete test rig for which a detailed description can be found in [36]. A cross-section of the actual chamber, i.e. the optically accessible measurement volume as well as the spray dump is given in Fig. 2. The former has a diameter of 110 mm and extends 40 mm in the direction of the spray axis, amounting to roughly 0.5 L of volume.

In the present investigation, the chamber is filled with technical air from compressed gas bottles which is prepared in the autoclave at a temperature of 673 K and a

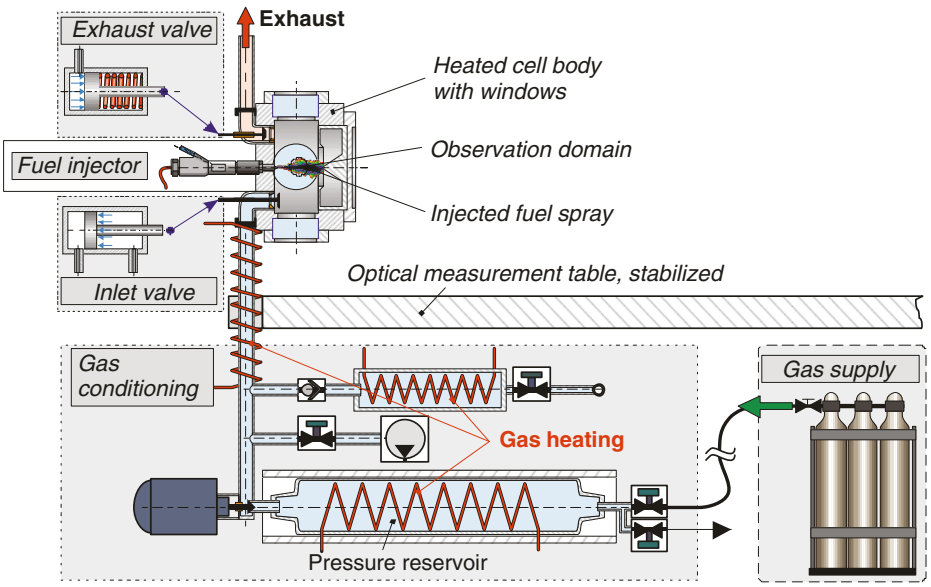


**Fig. 1** Schematic of the ETH high pressure high temperature cell test rig. Source [36]

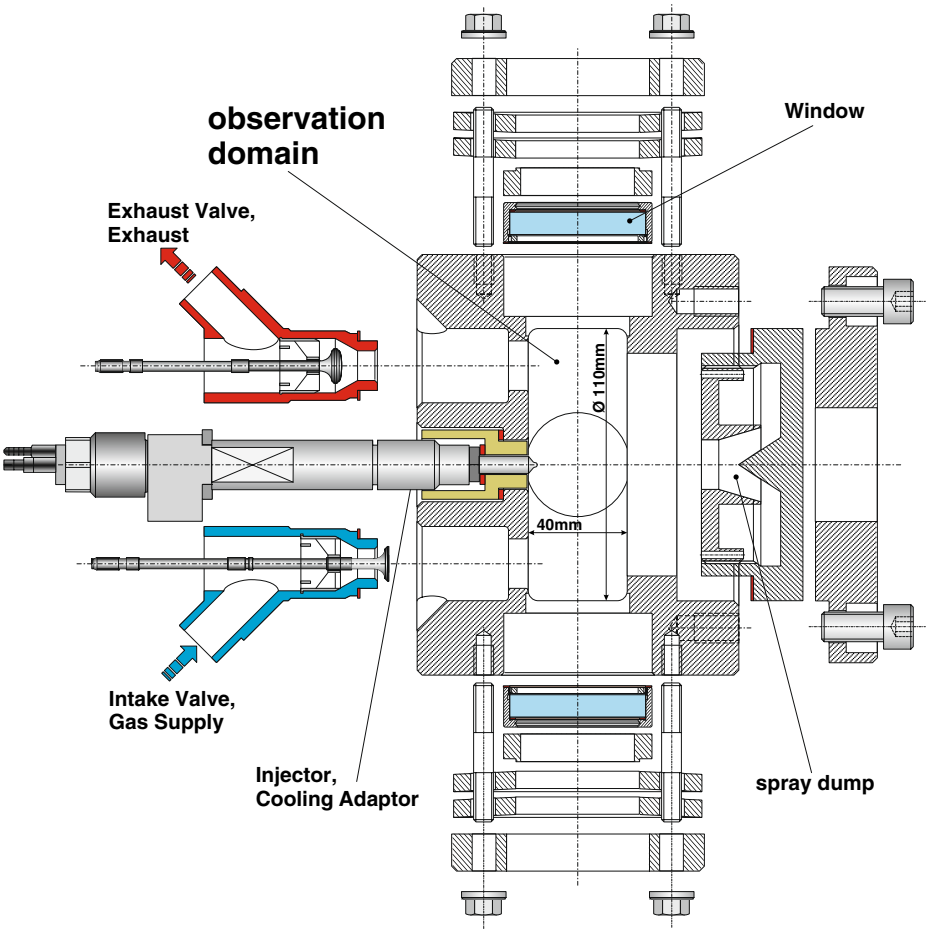


**Fig. 2** Schematic of the ETH high pressure high temperature chamber with indicated observation domain, fuel injector, air intake and exhaust paths, spray dump (two-piece assembly) and windows

pressure of 80 bars. The cell body and the intake pipe are heated by means of electric heating cartridges. Temperature sensors are installed at multiple locations and the control system of the rig can maintain temperatures of up to around 800 K, thereby ensuring a heat-up of the air from the autoclave to diesel engine conditions during the intake process. To obtain higher temperatures and pressure ranges than the ones used in this study, it is common practice, see e.g. also [11], to employ pre-combustion of $H_2/O_2/N_2$ which however leads to residual gases present in the chamber at the start of the experiment.

An overview of the operating conditions of the cell in the present study is given in Table 1. The apparatus is equipped with a common rail fuel injection system and a single-nozzle solenoid fuel injector. As is shown in Table 1, a very low injection pressure has been used, primarily with the aim of avoiding ignition of the spray outside the observable domain and, more importantly, to prevent forced ignition on the hot walls.

**Table 1** Operating conditions for the ETH high pressure high temperature cell

| | |
|---|---|
| Fuel type | *n*-heptane |
| Injection pressure | 320 bars |
| Injection duration | 1.80 ms (electrical), 1.65 ms (physical) |
| Total injected fuel mass | ~4.7 mg |
| Nozzle diameter | 0.15 mm |
| Nozzle L/D | 4 |
| Air pressure | 80 bars |
| Air temperature | 776 K |
| Wall temperatures | ~800 K |

The pressure in the chamber itself is recorded by means of a cooled piezo-electric pressure transducer (KISTLER 6061B) together with an absolute piezo-resistive transducer (KISTLER 4075A10) placed in the intake pipe. The spectrally and spatially integrated light emission has been recorded by means of a photomultiplier together with the pressure trace at a sampling rate of 200 kHz. Since the spray dump of the combustion chamber is optically not accessible, the observed fact, that the combustion related light emission slightly precedes the pressure rise due to the heat release rate, verifies that indeed the ignition location is within the visible part of the combustion chamber.

As diesel fuel contains a blend of various *n*-paraffins, olefines, aromatics and other hydrocarbons, chemical mechanisms are difficult to obtain and tend to be non-universal. To eliminate the influence of such uncertainties, *n*-heptane has been used as a fuel, which has a comparable cetane number to diesel and hence similar ignition behaviour. In addition, using heptane facilitates comparison with simulation, since chemical schemes for heptane are better developed than for diesel.

Optical access is gained in the two orthogonal directions transversal to the spray axis through the four side windows. Three types of optical measurement techniques have been employed which are described in the following section.

### *2.1.1 Schlieren imaging*

Schlieren imaging is a backlight technique which enables optical visualisation of variations in the refractive indices caused by density gradients, disturbances and inhomogeneities of transparent media. These small changes in the refractive indices compared to the homogeneous background cause bending of the illuminating light rays which allow visualisation of the gradients. A more detailed description of the broadly established Schlieren technique can be found in e.g. [37].

In the present investigation, the point light source consists of a xenon flash lamp masked by a pinhole. The emitted light is collimated by a first lens and subsequently passes through the spray axis in the combustion chamber. A second lens (NIKKOR 35 mm) is used to refocus the beam onto the camera; in the focal point a round knife-edge of 0.3 mm is placed to image the transparent Schlieren objects. A CCD camera (PCO) with a resolution of 1,280 × 1,024 pixels and a 12 bit dynamic range is used to record the images. A schematic of the set-up is given in Fig. 3. The exposure time was set to 700 ns in order to obtain sharp images of the fast injection process; the spatial resolution of the Schlieren images is approximately 40 μm.

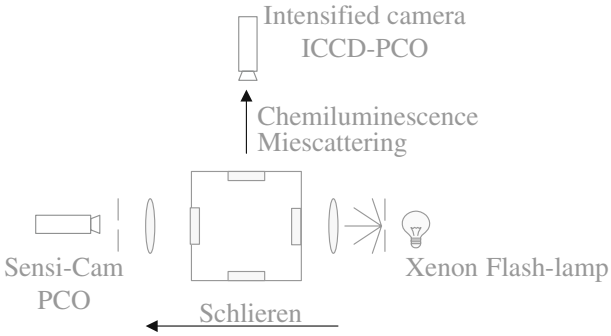


**Fig. 3** Schematic of the imaging arrangement for chemiluminescence, Mie scattering and Schlieren techniques

Due to the high sensitivity of the Schlieren method, it was necessary to inject the fuel into a quiescent environment. Strong turbulence within the measuring volume rendered the fuel spray unrecognizable due to the optical disturbances. Therefore, following the filling of the chamber with the pre-heated, high pressure air from the autoclave, turbulence is allowed to decay by waiting 2 s before starting the injection process. This duration has been motivated based firstly on qualitative Schlieren data at about the end of the intake process (not shown here) and secondly on an estimate of characteristic scales for both the decay of turbulent kinetic energy and the uptake of the heated wall temperature by the incoming gas. For the decay of turbulent kinetic energy, homogeneous and isotropic turbulence is assumed and the dissipation term is computed according to the standard parameters of the $k-\varepsilon$ model, whereas the integral length scale has been taken equal to the intake valve lift. The initial turbulence intensity has been estimated on account of the volumetric flow rate and the available valve cross section during intake as well as about 20% turbulence intensity yield out of the mean velocity at the valve; as is typical for intake-generated shear flows. Resulting decay times are—given all uncertainties of the simplified calculations—between 10 and 100 ms.

With regard to the wall heat transfer process, characteristic times for the given temperature uptake of the incoming gas by the walls are estimated using density and thermal capacity of the air, the volume-to-surface ratio of the chamber and heat transfer rates according to forced convection, while Nusselt, Reynolds and Prandtl numbers are computed according to the properties of air at given pressure and temperature as well as to the estimated flow velocities. Resulting temperature uptake times are of the order of a few 100 ms. Therefore one can conclude, that after 2 s from the end of the intake process, the flow can be assumed to be almost totally quiescent in terms of turbulent kinetic energy and the gas temperature to be rather homogeneously distributed at (approximately) the level of the heated wall temperature.

During this period, small decreases in the cell temperature and hence pressure have been reported in [36]. The three major sources of these heat losses are the valves, the fuel injector and the pressure transducer. With the exception of the latter, all these components require extra cooling as the cell operation is intermittent and no cooling due to scavenging with relatively cold air can take place as in reciprocating arrangements. Although not actively heated, the windows in contrast are at very high temperatures due to the high conductivity of sapphire.

### *2.1.2 Chemiluminescence measurement technique*

Chemiluminescence is a photon-emission phenomenon that appears throughout the diesel combustion process. It arises from certain energetic chemical reactions which lead directly to the formation of atoms or molecules in an electrically excited state. Such radicals may decay back to equilibrium energy levels thereby emitting photons. By using appropriate interference filters (narrow band pass $310 \pm 2$ nm), it is possible to detect the emission intensity of OH* radicals in electronically excited states which serve as a tracer of the heat release rate and hence the ignition location if spatially resolved.

In order to accomplish simultaneous imaging of chemiluminescence and Schlieren, two cameras are used with orthogonal lines of sight through both pairs of opposing cell windows in the transversal spray directions. The two pictures are taken on two different axes (90° of difference) to avoid the adoption of a beam splitter. Due to the low intensity of the chemiluminescence signal, a 16 bit intensified CCD camera with $640 \times 512$ pixels (PCO SensiCam) and a NIKKOR 105 mm UV-lens are used to take the images. A schematic overview of the configuration is shown in Fig. 3. For both techniques the trigger delay is the same, i.e. the images are taken simultaneously. The exposure time of the camera was set to 7.0 μs.

### *2.1.3 Mie scattering*

Mie scattering occurs when the particles have the same size or slightly larger than the wavelength of radiation in contact with them. The Mie theory provides exact solutions of scattered intensity from spherical particles to a given angle. Mie scattering signal is obtained from scattering of the xenon flash lamp light radiation by the fuel droplets. During injection process some of the light (xenon flash lamp) will be elastically scattered by the liquid fuel droplets. Collecting this scattered light allows the liquid fuel distribution to be visualised. The set up and the parameters used to record the Mie scattering images are the same as the one of chemiluminescence.

The Mie scattering uses the same ICCD camera and set-up as for the chemiluminescence imaging shown in Fig. 3. The camera exposure time is set to 20 μs and the spatial resolution is approximately 80 μm.

### *2.1.4 Air initial temperature measurement*

To accurately measure the air temperature prior to injection, a Philips Thermocoax thermocouple with a tip diameter of 0.25 mm is permanently located inside the chamber. It is of the Alumel/Chromel K-type, with a typical response time of less than 1 s in quiescent air [38]. As injection is delayed 2 s after filling the cell in order to allow for turbulence to decay, this ensures an accurate measurement of the initial gas temperature inside the chamber. To avoid touching the spray during injection, it is placed slightly off-centre towards the exhaust valve side. In [36] it was shown, that while the precision of the thermocouple is very high (to within a few kelvins), the bias is estimated to be around ±3% at the conditions considered.

### *2.1.5 Fuel injection*

No time-resolved fuel injection rate measurements were carried out; however the needle lift was recorded. The total injected fuel mass was determined by repeating

one thousand injections into a closed vessel and determining the weight difference on a high accuracy balance to obtain an arithmetic mean of the total injected fuel mass.

## 3 Numerical Methodology

The numerical set-up consists of a commercial flow field solver, STAR-CD [39] for computational fluid dynamics (CFD), coupled to an elliptic CMC based combustion code. Details concerning the latter, as well as the coupling can be found in [33, 34].

### 3.1 CMC formulation

Detailed derivations of the governing equations for CMC have been proposed in [40–42]. Conditional expectations of species mass fractions, $Q_\alpha$, and temperature, $Q_T$, are defined as ensemble averages with respect to $\xi$ fulfilling the following condition:

$$\langle \cdot | \xi(\mathbf{x}, t) = \eta \rangle \tag{1}$$

where $\eta$ is the sample space variable for the conserved scalar. Hence:

$$Q_\alpha(\eta, \mathbf{x}, t) = \langle Y_\alpha(\mathbf{x}, t) | \xi(\mathbf{x}, t) = \eta \rangle \,, \tag{2}$$

$$Q_T(\eta, \mathbf{x}, t) = \langle T(\mathbf{x}, t) | \xi(\mathbf{x}, t) = \eta \rangle \,. \tag{3}$$

By adopting the assumptions from [42] of high Reynolds and unity Lewis numbers, the following transport equations for the conditional species mass fractions and temperature are obtained:

$$\frac{\partial Q_\alpha}{\partial t} + \langle u_i | \eta \rangle \frac{\partial Q_\alpha}{\partial x_i} - \langle N | \eta \rangle \frac{\partial^2 Q_\alpha}{\partial \eta^2} + \frac{1}{\bar{\rho} \tilde{P}(\eta)} \frac{\partial}{\partial x_i} \left[ \left\langle \rho u_i'' Y_\alpha'' | \eta \right\rangle \tilde{P}(\eta) \right] = \langle w_\alpha | \eta \rangle \,, \tag{4}$$

$$\begin{aligned} \frac{\partial Q_T}{\partial t} + \langle u_i | \eta \rangle \frac{\partial Q_T}{\partial x_i} = {} & \langle N | \eta \rangle \frac{\partial^2 Q_T}{\partial \eta^2} + \langle N | \eta \rangle \\ & \times \left[ \frac{1}{\langle c_P | \eta \rangle} \left( \frac{\partial \langle c_P | \eta \rangle}{\partial \eta} + \sum_{\alpha=1}^{N} \langle c_{P,\alpha} | \eta \rangle \frac{\partial Q_\alpha}{\partial \eta} \right) \right] \frac{\partial Q_T}{\partial \eta} \\ & - \frac{1}{\bar{\rho} \tilde{P}(\eta)} \frac{\partial}{\partial x_i} \left[ \left\langle u_i'' T'' | \eta \right\rangle \bar{\rho} \tilde{P}(\eta) \right] + \frac{1}{\langle c_P | \eta \rangle} \left\langle \frac{1}{\rho} \frac{\partial P}{\partial t} \middle| \eta \right\rangle \\ & + \frac{\langle w_H | \eta \rangle}{\langle \rho | \eta \rangle \langle c_P | \eta \rangle} + \frac{\langle w_{\mathrm{WALL}} | \eta \rangle}{\langle \rho | \eta \rangle \langle c_P | \eta \rangle}. \end{aligned} \tag{5}$$

Standard modelling practice has been followed for the unclosed terms: The conditional turbulent flux has been modelled using a gradient transport assumption, the linear model is used for the conditional velocities and the Amplitude Mapping

Closure (AMC) is employed to model the conditional scalar dissipation rate $\langle N|\eta\rangle$ [42]. Wall heat transfer has been modelled as suggested in [43] as:

$$\langle w_{\mathrm{WALL}}|\eta\rangle = \alpha\left(Q_T - \tilde{T}_{\mathrm{WALL}}\right);\ \text{with}\ \alpha = \frac{\dot{q}^{\mathrm{CFD}}_{\mathrm{WALL}}}{\int\limits_0^1 \left(Q_T - \tilde{T}_{\mathrm{WALL}}\right)\tilde{P}(\eta)\,d\eta} \tag{6}$$

where $\dot{q}^{\mathrm{CFD}}_{\mathrm{WALL}}$ denotes the wall heat flux from the CFD solver. The conditional source terms from chemical reactions are closed at first order. Investigations employing second order closure have been presented in [30, 44]; due to the strong increase in computational cost conditional fluctuations have been neglected in the present investigation to enable the multitude of runs required for the sensitivity analyses. As discussed in more detail in [30, 45], first-order closure has been shown to be sufficient for auto-ignition in cases where the scalar dissipation rate rapidly decays to sub-critical values. Nonetheless, future, more detailed investigations should assess the importance also for the present conditions as conditional fluctuations could—in principle—play a role for this spray.

Droplet evaporation has not been accounted for in the present formulation, although various attempts to include such effects either in the CMC and/or mixture fraction variance equations have been proposed [32, 46–48]. Newer developments for dispersed solid phase combustion have been presented in [49] where it is proposed that the approach can in principle also be used for liquid fuel sprays. A rigorous derivation addressing the implications of two-phase flows in the CMC framework in detail recently appeared in [50]. It is evident, that further efforts are still required towards fully incorporating the effect of droplets in the CMC equations and the mixture fraction variance.

### 3.2 CFD solver

The flow field solver uses a locally refined, hexahedral cylindrical grid as shown in Fig. 4. As the spray is injected along the axis of symmetry, a quasi-2D grid has been employed. The PISO based solver is chosen; time integration is performed with the standard implicit Euler formulation using a constant time step of $1.0 \times 10^{-6}$ s. Turbulence is modelled by the RNG variant of the two-equation $k - \varepsilon$ model without any adjustment of the default constants. Spray atomisation is modelled by the Huh model [51] and alternatively by the Reitz–Diwakar model [52], for which a cone angle must be prescribed. Secondary break-up is treated by the Reitz–Diwakar model in both cases and all model constants are set to their default values. Despite the unlikely impingement of droplets on solid walls the splashing model of Bai has been employed, for which documentation can be found in [53]. The thermo-physical properties of the droplets (viscosity, density, latent heat, $c_p$, surface tension and saturation pressure) are computed internally in STAR as functions of temperature.

Thermodynamic properties of the species are prescribed by polynomial representations of the respective specific heats at constant pressure. Enthalpy in STAR-CD is solved in the form of the total enthalpy; hence no transport equations for the mean species mass fractions are required in the flow-field solver, as the species mass fractions are computed by the CMC. A β-function has been presumed for the

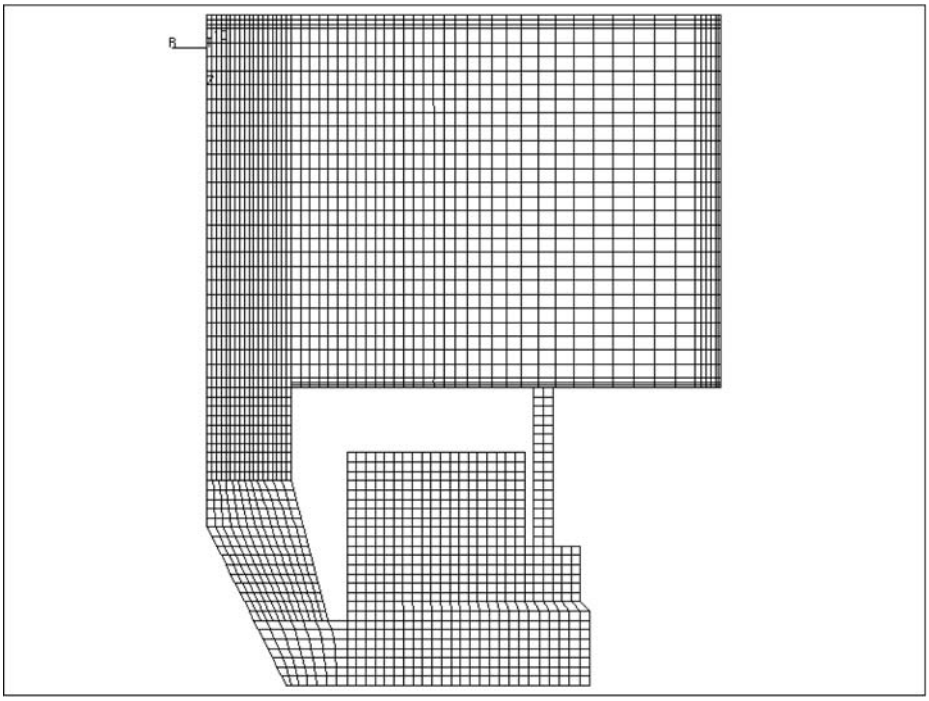

**Fig. 4** CFD grid of the combustion chamber and spray dump

PDF, governed by two moments, namely the Favre averaged mixture fraction and its variance, which obey the following transport equations:

$$\frac{\partial \bar{\rho}\tilde{\xi}}{\partial t} + \nabla\left[\bar{\rho}\tilde{u}_j\tilde{\xi} - \left(\bar{\rho}D_{\tilde{\xi}} + \frac{\mu_t}{Sc_{\tilde{\xi}}}\right)\nabla\tilde{\xi}\right] = \dot{S}_d, \tag{7}$$

$$\frac{\partial \bar{\rho}\widetilde{\xi''^2}}{\partial t} + \nabla\left[\bar{\rho}\tilde{u}_j\widetilde{\xi''^2} - \left(\bar{\rho}D_{\widetilde{\xi''^2}} + \frac{\mu_t}{Sc_{\widetilde{\xi''^2}}}\right)\nabla\widetilde{\xi''^2}\right] = \frac{2\mu_t}{Sc_{\widetilde{\xi''^2}}}\left(\nabla\tilde{\xi}\right)^2 - \bar{\rho}\tilde{\chi}. \tag{8}$$

While the former includes a source term on the right hand side (RHS) to account for the influence of the evaporating droplets, the latter is modelled following standard practice, i.e. neglecting the influence of droplet evaporation as a clear consensus hereto is not yet established as is discussed in the previous section.

The mean scalar dissipation rate is computed from the mean turbulence quantities as follows:

$$\tilde{\chi} = c_\chi \frac{\tilde{\varepsilon}}{\tilde{k}}\widetilde{\xi''^2}. \tag{9}$$

Following common practice, a prescribed value of 2.0 has been used for the model constant $c_\chi$; although sensitivity with respect to this quantity has been reported in [46, 54].

### *3.2.1 Numerical method*

The CMC equations (4) and (5) are discretised using finite differences. An upwind scheme has been used for the first and centred differences for the second derivatives in physical and $\eta$-space. The conserved scalar space grid has 101 nodes which are clustered around the stoichiometric value of 0.062. Ignition can be expected to take place at the 'most reactive' mixture fraction, $\xi_{MR}$, [55]. As shown in [33, 34], values in the range of 0.08 to 0.1 were evaluated for auto-ignition calculations with homogeneous CMC at diesel engine conditions, which is sufficiently close to this high resolution region. However the exact value of $\xi_{MR}$ is dependent on the configuration, e.g. air and fuel temperatures, scalar dissipation rate and the chemical mechanism considered.

The allocation of the CFD nodes to the CMC grid uses a fully automated procedure for which the methodology is discussed in detail in [34, 44]. The spatial resolution of the CMC grid is 40 and 23 nodes in the radial and axial direction respectively. Therefore, in the region of interest, there are around two CFD cells mapped to one CMC node. A weighting with respect to the PDF is employed where multiple CFD cells are assigned to one CMC node.

For efficient integration of the CMC equations, an operator splitting approach has been followed. As argued in [33], if sufficiently small time steps are used, the associated errors and hence the influence on the simulation results are small. In [34, 44], the approach from [33], which separated the physical space transport from the joint chemical reaction and molecular mixing in conserved scalar space, has been further extended to three sub-steps by further splitting the latter two processes. A sensitivity analysis for the validity of this approach and the associated substantial gains in computational efficiency are discussed in detail in [44].

### *3.2.2 Chemical mechanisms*

For *n*-heptane various skeletal or reduced mechanisms have been reported in the literature, e.g. [56–59]. Based on the detailed mechanism of [57] with 67 species, a reduced mechanism has been proposed by Bikas [58]. It has a total of 59 species, of which 28 are set to steady state based on computational singular perturbation concepts. This mechanism has shown good agreement in previous studies of auto-igniting *n*-heptane sprays [33] and in diesel engine simulations [34]. To assess the influence with respect to the chemistry employed the reduced mechanism from [59] has also been assessed. It is derived from a skeletal mechanism with 43 species and 185 reactions which, by introducing steady state assumptions, is further reduced to only 18 steps and will be referred to as the Liu et al. mechanism.

Both mechanisms have been validated (in [33] and in [59], respectively) in terms of ignition delays for homogeneous mixtures at different equivalence ratios, temperatures and pressures by means of experimental data from [60].

## 4 Results and Discussion

### 4.1 Experiments

Figure 5 shows the recorded pressure traces of 17 realisations of the experiment. The raw pressure data has been smoothed within the individual cycle by applying

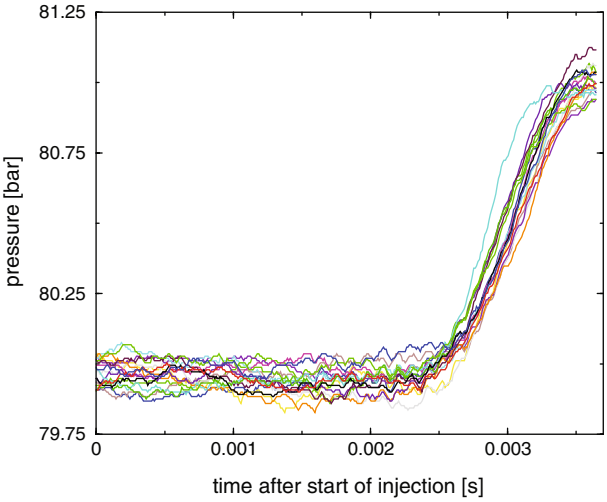


**Fig. 5** Recorded pressure traces for 17 individual realisations; sample rate is 200 kHz. The raw data has been smoothed by 50-point running averages. Total injection duration 1.65 ms (physical)

a running averaging procedure over 50 points of the 0.005 ms sampling rate. The overall pressure increase amounts to only roughly one bar, which is small compared to the initial pressure of 80 bars due to the small quantity of fuel injected and the global equivalence ratio of over 40, but is nonetheless measurable. The slight decrease in pressure from the start of injection (SOI) until the time of ignition is due to small heat losses discussed above.

The standard deviation in the raw pressure signals at the start of injection amounted to 0.21 bar, which corresponds to roughly 0.26% of the initial pressure of 80 bars. Similar considerations apply at the end of the pressure rise, where the deviation was 0.243 bar or roughly 0.3%. Ignition occurs at around 2.5 ms based on the chemiluminescence images which will be discussed below. Based on a threshold of 80.125 bars, at 2.7 ms the differences in the delays based on the pressure traces were within less than $\pm 0.1$ ms, which corresponds to an RMS over mean of about 4%. This is in contrast to the findings reported in [6], where strong variability was reported which was attributed to small spatial and temporal temperature in-homogeneities, estimated to be of the order of 20 K. In [7], the statistical analysis of around 200 repetitions of auto-igniting *n*-octane sprays in a shock-tube also showed a significant spread of the induction period around the mean. For auto-igniting jets of gaseous DME presented in [61], the 95% confidence intervals for the ignition delays amounted to roughly a quarter of the total delay. For the model engine in [1], ignition delays and their standard deviations averaged from roughly 100 cycles are reported for nine different operating conditions. For the majority of the conditions the ratio between the standard deviation and average ignition delay spanned 20% to 30%. Based on the experimental data obtained in the present investigation, it can be hence concluded, that for our closed experimental configuration, the initial air temperature is highly constant for the majority of the realisations. From Fig. 5 it is also evident, that the rate of change of the pressure following ignition is very reproducible, i.e. the slope is almost identical for most realisations, which gives credence to highly repeatable injection rates and total amount of fuel injected.

Figure 6 shows the evolution of the liquid phase spray penetration by means of Mie scattering, which exhibits stagnation behaviour. Furthermore, it is evident, that the slope of the injection rate is extremely high as the liquid core is fully developed within the first 0.3 ms and, likewise, ends very abruptly. The gas phase spray penetration displayed in Fig. 7 by means of single shot images however continues to advance throughout the entire chamber and enters the spray dump at around 1.3 ms. Such findings are typical of high pressure sprays at evaporating conditions and in agreement with other studies, e.g. [1, 3, 13, 36]. For quantitative values, it is common practise to perform averaging of numerous single shot images and the definition of the spray tip penetration is then often based on the 5% extinction. No attempt has been made here to obtain such values as the evolution of the gas phase spray will serve solely for qualitative comparisons and adjustment of spray model constants. More rigorous experimental studies including also droplet sizes and velocities for accurate comparisons have been presented in [36], whereas investigations reporting quantitative fuel vapour distributions can be found e.g. in [62]. Despite allowing for the turbulence to decay by waiting for 2 s following the gas intake process, in addition to the strong changes in the spray region, significant variations in the refractive indices can still be observed in the entire chamber (cf. Fig. 7). These are mainly due to gradients in temperature as a consequence of the hot/cold areas as discussed above leading to buoyancy driven flow patterns, as was also seen in [63]. No measurements of velocity field and fluctuations were available for the estimation

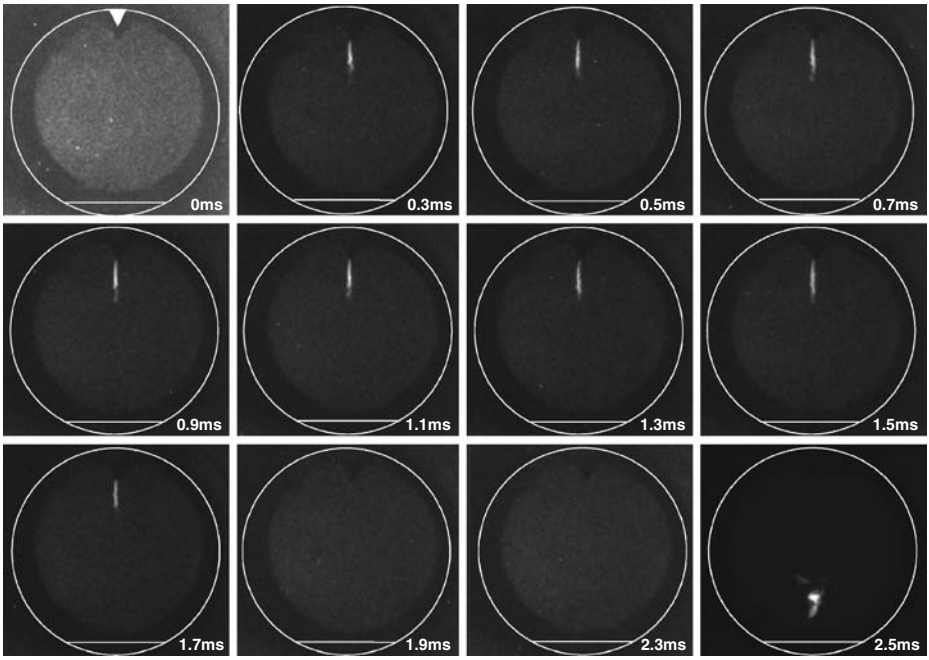


**Fig. 6** Evolution of Mie-scattered light. The *white circle* shows the cell window, the *straight line at the bottom* the location of the wall. The first image was used for background subtraction from the following images and depicts the location of the injector at the *top*

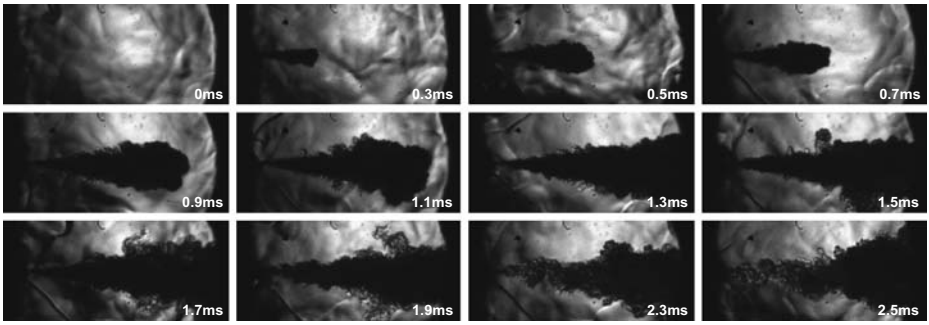


**Fig. 7** Evolution of the fuel gas phase penetration by means of Schlieren imaging

of turbulence quantities at the start of injection. Future investigations could hence employ high-speed PIV systems to collect such data for input as initial conditions to the simulation.

While the ignition timing is highly repeatable, from a selection of chemiluminescence images given in Fig. 8, substantial variability in the location of first ignition is evident. This is further illustrated by the computed mean and RMS from a total of 48 realisations thereof, which are displayed in Fig. 9; the former quantity will serve as a qualitative comparison for the numerical investigations. As the camera is always triggered at the same time (2.5 ms), even small differences in ignition delay manifest themselves in large differences in the intensity of the chemiluminescence images. Experimental evidence of such randomness in the ignition location has also been reported e.g. in [1, 7]. As the ignition delay reported in [1] exhibited substantial variations, it is however unclear to what extent the differences in the location can be attributed to the differences in ignition timing, i.e. if the two can be independently considered. For engines with multi-hole nozzles on the other hand, one single injection event for a given engine cycle provides a 'collection' of auto-ignition sites for each of the fuel sprays (which are at 'identical' thermodynamic conditions), as can be observed in the study of [4], where the influence of cycle-to-cycle variations is additionally presented. In [61], investigations of the mixture fraction distribution of gaseous DME jets by means of LIF enabled the calculation of discrete mixture fraction PDFs. Conjectures employing the flammability limits of the fuel allowed for a subsequent derivation of iso-contours indicating a local ignition probability. Areas with high probability cover a wide range of locations along the developing jet periphery. The randomness of the ignition location within these likely regions observed is attributed to temperature and flow field inhomogeneities which were however not taken into account in the derivation of the probability contours.

On the numerical side, investigations by means of DNS of auto-ignition using one step [55] and detailed chemistry [64] have shown, that ignition always occurs along iso-levels of the mixture fraction at its most reactive value with low levels of the scalar dissipation rate. Due to the influence of turbulence, each individual realisation of an injection event can be expected to have a different distribution of these iso-levels and hence a substantial randomness can be expected as far as the location of the ignition spot is concerned. However, as the full range of scalar dissipation rates is likely to be present along a most reactive mixture fraction iso-contour (independent

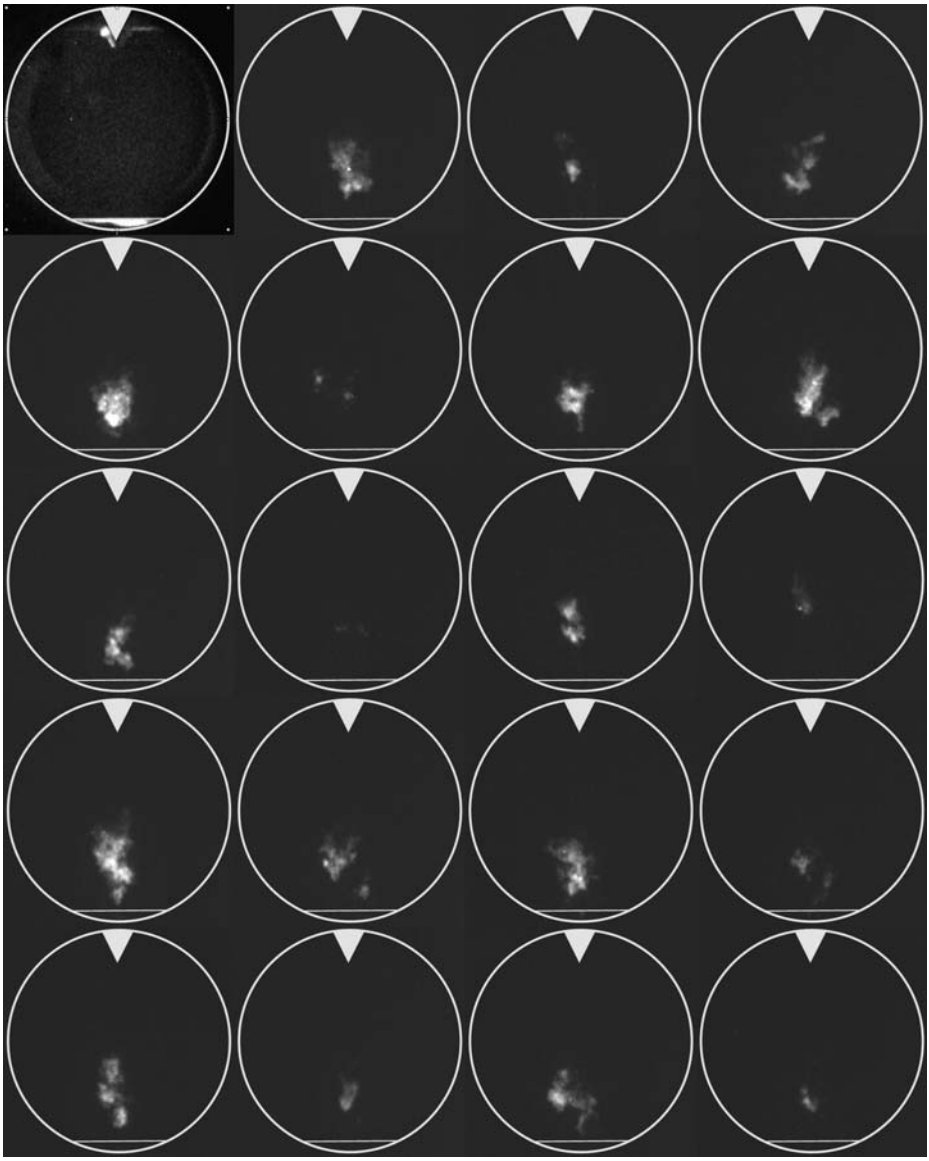

**Fig. 8** Selection of 19 chemiluminescence images at the time of ignition (2.5 ms after start of injection) showing the substantial variation of the ignition location. The *top left image* has been used for background subtraction and to determine window, injector and wall locations shown by the *ring*, *triangle* and *line*, respectively

of its location), a time history for such a combination is conceivable such that the ignition delay is only moderately affected. This argument is fully consistent with the very small variation of ignition time, despite the large variation of ignition location. Further discussion on the subject can be found in [45].

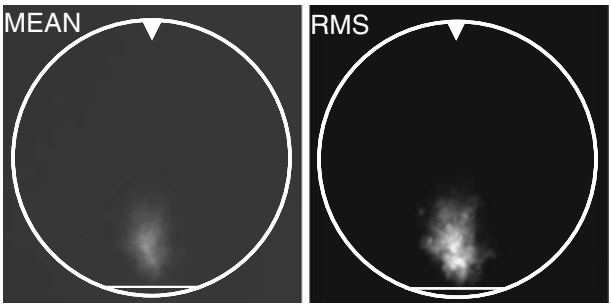


**Fig. 9** Chemiluminescence signal mean (*left*) and RMS (*right*) computed from 48 individual realisations. Window, injector and wall locations shown by the *ring*, *triangle* and *line*, respectively

## 4.2 Numerical predictions and sensitivity analysis

### *4.2.1 Chemical mechanism comparison*

Investigations by means of stand-alone "flamelet" ignition calculations at the nominal conditions, i.e. 80 bars and 776 K, are given in Fig. 10. A systematic difference in the ignition delay is evident for prescribed peak scalar dissipation rates $\langle N|\eta = 0.5\rangle$ up to a value of around 25 $s^{-1}$, which can be attributed to the mechanism. At higher values, the 'slower' Liu et al. chemistry cannot balance diffusion in conserved scalar space and hence shows a critical scalar dissipation rate almost an order of magnitude lower than the Bikas mechanism.

For a prescribed peak scalar dissipation rate $\langle N|\eta = 0.5\rangle$ of 10 $s^{-1}$, the evolutions of the heat release rate and the temperature at the stoichiometric mixture fraction have been evaluated which are shown in Fig. 11. The Bikas mechanism predicts a heat release rate almost one order of magnitude higher than the Liu et al. chemistry throughout the entire ignition phase. At the time of ignition (1.484 ms for the Bikas mechanism, 2.238 ms for the Liu et al. mechanism), the cumulative heat released at stoichiometry however are very comparable and the temperatures attained almost identical.

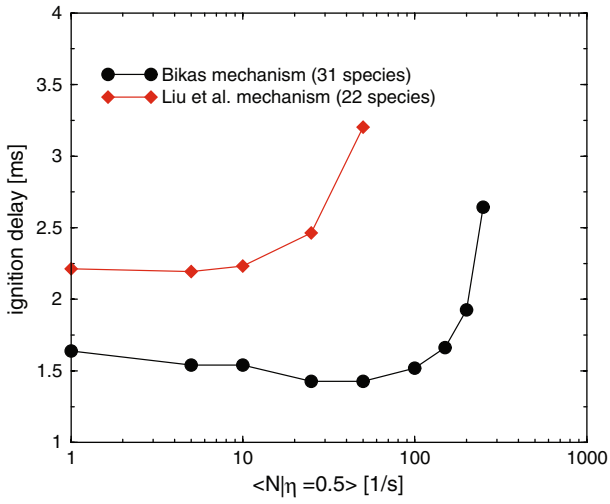


**Fig. 10** Ignition delay comparison for stand-alone 0D-CMC ignition calculations with the reduced chemical mechanisms for *n*-heptane from Bikas [58] and Liu et al. [59] at 80 bars, 776 K air and 300 K fuel boundary temperatures. The conditional scalar dissipation rate has been modelled with the AMC model [42] for which the peak value $\langle N|\eta = 0.5\rangle$ is prescribed

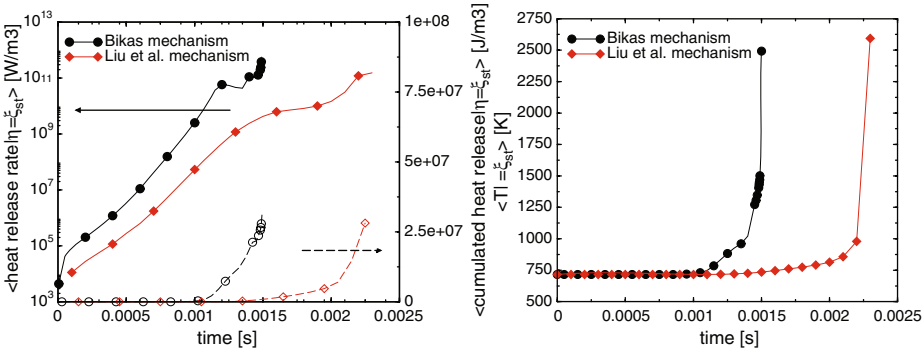


**Fig. 11** Time evolutions of the conditional heat release rate and the cumulated heat release at stoichiometry (*left*) and the conditional temperature at stoichiometry (*right*) for the mechanisms of Bikas [58] and Liu et al. [59]

To further assess the differences between the two mechanisms, the conditional temperature, conditional heat release rate and the conditional species mass fractions for a selection of scalars have been compared, cf. Fig. 12. Shortly before ignition the conditional temperature profile is broader for the Liu et al. chemistry, which can

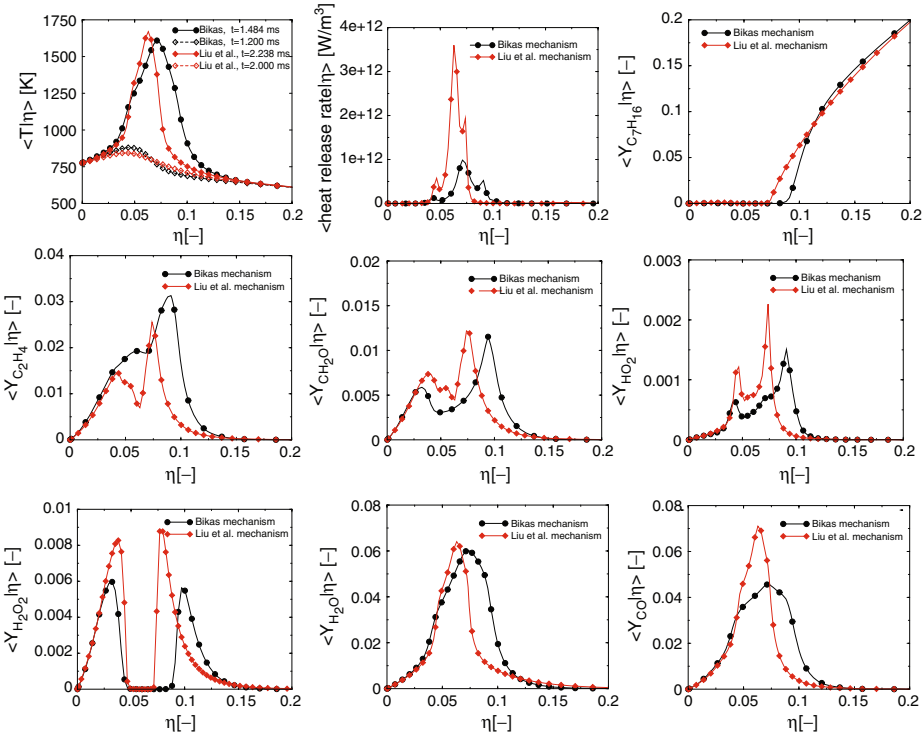


**Fig. 12** Conditional temperature, conditional heat release rate and a selection of conditional species mass fractions at the time of ignition (1.484 ms for the Bikas [58], 2.238 ms for the Liu et al. [59] mechanism)

be expected for this reaction-diffusion system due to the smaller chemical i.e. heat source but identical molecular mixing (acting as the diffusion term). At the time of ignition, the temperature profile for the Bikas chemistry is broader as more fuel has been converted to intermediates and the most reactive mixture fraction is located slightly on the rich side ($\xi_{MR} \approx 0.072$). Three peaks can be observed in the conditional heat release rate and the OH mass fraction: One at stoichiometry and, additionally, a lean and a rich branch which will spread towards the respective boundaries consuming the premixed portions of the mixture. On the lean side, the peaks in the $HO_2$ and $H_2O_2$ radicals agree very well both in terms of location as well as magnitude. The same also applies to the OH radical (not shown as it follows qualitatively the heat release rate) and two selective intermediates, $C_2H_4$ and $CH_2O$. The profiles of two products, $H_2O$ and CO, which only exhibit one peak around stoichiometry, also show good agreement on the lean side up to values of around $\xi \approx 0.05$.

#### *4.2.2 Liquid and gas phase spray penetration*

In a first step, the liquid and gas phase spray penetrations are compared with the experimental data. The stagnation behaviour of the liquid phase discussed earlier was correctly captured by the simulation, which is in agreement with findings reported in previous investigations [65, 66] validating the same flow field solver against data from the same cell for evaporating diesel sprays [36]. A merely qualitative comparison of the evolution of the gas phase of the spray is presented by comparing the fuel mass fraction iso-contours and overlaid droplets with single-shot Schlieren images in Fig. 13. Overall, the agreement with the experimental data is reasonable, and depends on the spray model utilised. The Reitz–Diwakar with 5° cone angle slightly over predicts the penetration at most stages, while the 8° cone angle shows good agreement in particular at the early stages, where a small under prediction is visible for the Huh model (which predicts the spray cone angle). The latter however agrees best at the later stages.

#### *4.2.3 Ignition delay and pressure rise*

Figure 14 shows the predicted pressure rise for the two different chemical mechanisms for various initial temperatures using the injection rate based on the needle lift and the Huh atomisation model. As no special care has been taken to model the heat losses through the cooled valves, injector and pressure transducer, the slight pressure decrease between start of injection and the time of ignition which can be seen in the experiment (cf. Fig. 5) is not captured by the simulation. Both mechanisms accurately reproduce the total pressure increase due to the heat released by the combustion. At the nominal temperature of 776 K, the shapes of the pressure traces during the initial, premixed phase agree well with the measurements and the following slope is also quite well predicted by both chemistries.

In the simulation, the definition of the ignition delay is arbitrarily taken as the time, when the Favre averaged temperature first exceeds 1,600 K. This is based on the consideration, that the high temperature regions are responsible for the experimentally detectable chemiluminescence signal. At the nominal temperature, the Liu et al. chemistry accurately predicts an ignition time of 2.6 ms, while the Bikas mechanism with 1.79 ms under predicts this value by roughly 30%, which is expected due to the large differences in the chemistry discussed previously.

In the experiment of [6] it was estimated that the temperature measurement uncertainty amounted to a maximum of 20 K, while for the present rig the error in the temperature measurement was found to be of the order of ±3% [36]. In engine calculations however, where the initial temperature in the chamber at intake valve closure (IVC) is commonly derived by means of thermodynamic considerations based on values measured in the intake manifold, the situation is far less clear than in such well-controlled environments. The sensitivity with respect to the initial temperature has therefore been assessed by decreasing the experimental value by 11 K for both mechanisms and for the Bikas chemistry also by 21 K, which corresponds to roughly 1.5% and 3% of the measured value, respectively. As can be seen in Fig. 14, lowering the temperature significantly delays the ignition as expected since we are below the negative temperature dependence regime and also lowers the heat release rate for both mechanisms as can be seen from the decrease in the rate of pressure rise. The overall increase in pressure is, however, captured well for all temperatures.

The influence of the initial air pressure was also assessed. To this end, two calculations with ±10% of the initial value were performed. The ignition delays were affected less than 2% and the ignition location was not affected.

As no experimental data for the injection rate was available, the sensitivity with respect to this intermittent boundary was investigated. The first approximation for the injection rate is based on the recorded needle lift signal, which is commonly employed as a first guess in the absence of measured data (which is often the case in engine configurations in particular). The second estimate for the fuel injection rate is based on the rate measurements reported in [36] for the same injector however using diesel fuel. It was there seen, that for small diameters the single bore can constitute the limiting cross-section even at very small needle lifts of around 0.05 mm. Hence the flow rate remained almost constant throughout the duration of the entire injection process and in particular was largely independent of the further travel of the needle. Therefore for this specific arrangement, a square injection rate profile has alternatively been assessed. The results from this sensitivity investigation are displayed in Fig. 15: While ignition in the case of the Bikas chemistry occurs around 1.63 ms, for the Liu et al. mechanism it is reduced to 2.47 ms which corresponds to a reduction of 9% and 5%, respectively. The pressure predictions are affected contrarily, i.e. steepened for the former and reduced for the latter. Due to the improved agreement of the needle lift approximation and given the uncertainty due to lack of experimental data, the needle lift profile has been employed for all future sensitivity analyses.

Initial turbulence in the background air can have a large effect on the ignition delay as has been shown in [5] and numerically reproduced in [33]. While great care has been taken to ensure quiescent conditions in this experiment, the temperature gradients between the ‘cold’ valves, injector and pressure transducer and the ‘hot’ walls of the cell lead to flow structures in the chamber as previously discussed. To assess the influence of very small amounts of turbulence which could hence be present, a calculation has been performed using the Huh atomisation model at

**Fig. 13** Vapour phase penetration evolution comparison: Schlieren images (*first column*) vs. fuel vapour iso-contours for Huh (*second column*, [51]) and Reitz–Diwakar model [52] with 5° (*third column*) and 8° (*fourth column*) cone angle. The superimposed droplets are coloured by temperature ▶

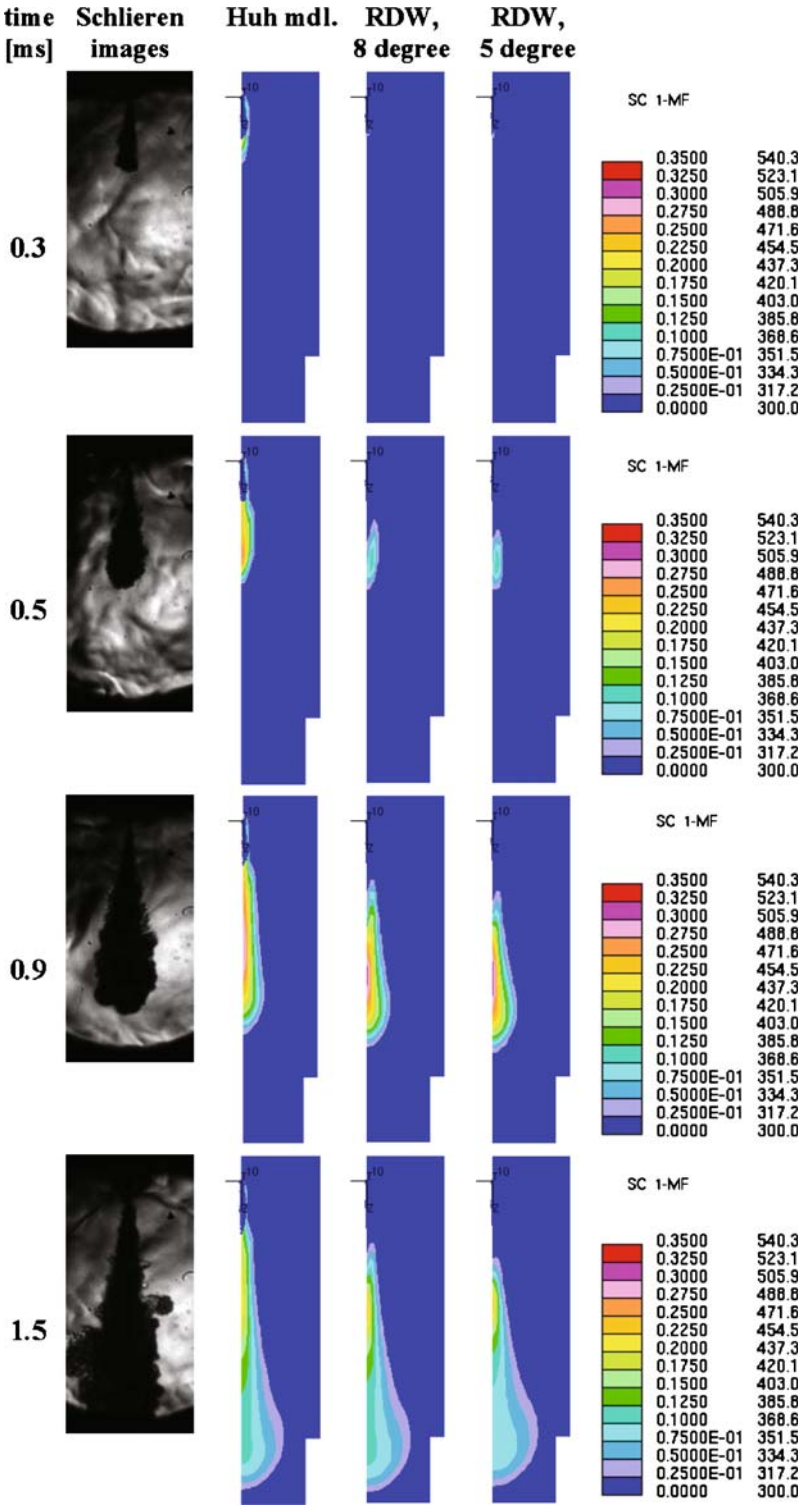
time [ms]
Schlieren images
Huh mdl.
RDW, 8 degree
RDW, 5 degree
0.3
0.5
0.9
1.5
SC 1-MF
0.3500 540.3
0.3250 523.1
0.3000 505.9
0.2750 488.8
0.2500 471.6
0.2250 454.5
0.2000 437.3
0.1750 420.1
0.1500 403.0
0.1250 385.8
0.1000 368.6
0.7500E-01 351.5
0.5000E-01 334.3
0.2500E-01 317.2
0.0000 300.0

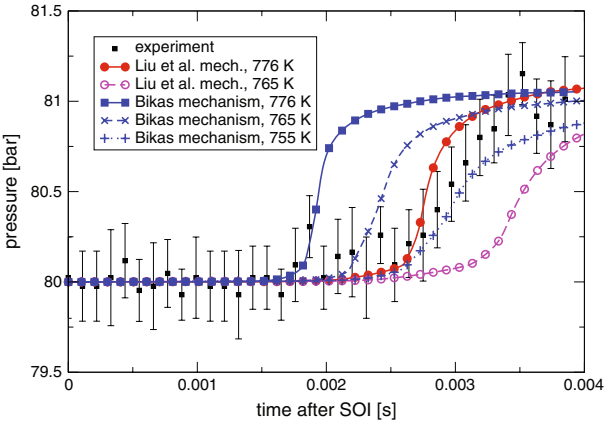


**Fig. 14** Pressure variation with time for various initial air temperatures and two chemical mechanisms [58, 59]. The Huh atomisation model [51] has been used

the nominal temperature and the Liu et al. mechanism with a prescribed initial turbulence intensity of 0.05 and an integral length scale of 0.01 m. The remaining mean velocity due to inflow and buoyancy has been estimated at a low value of only 1 m/s based on the considerations discussed above of an almost fully quiescent flow 2 s after intake valve closure. With an assumed low value of the turbulence intensity of only 5%, small fluctuations of 5 cm/s hence remain; the assumption of the integral length scale of 10 mm is based on the valve lift (which further coincides with roughly one tenth of the diameter of a sphere with a volume corresponding to the chamber). As shown in Fig. 16 for these low turbulence levels, hardly any influence on the ignition delay is evident, only small differences in the early, partially premixed phase can be observed.

Only a small influence of the atomization model on the ignition delay is evident from Fig. 17 for both mechanisms. Investigations concerning the overall evaporation and Sauter Mean Diameters (SMD) showed, that the Huh model (which predicts a droplet size distribution instead of uniform 'blobs') has significantly enhanced evaporation due to the smaller SMDs. Despite the difference in the prescribed cone angles, evaporation turned out to be very similar in the case of the Reitz–Diwakar model.

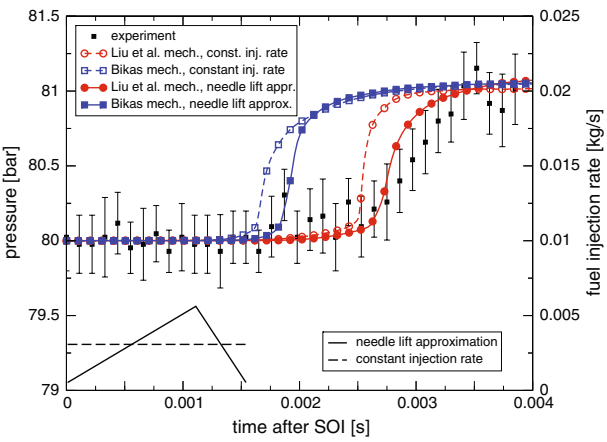


**Fig. 15** Pressure variation with time for two injection rate approximations and both chemical mechanisms [58, 59] at the nominal temperature. The Huh atomisation model [51] has been used

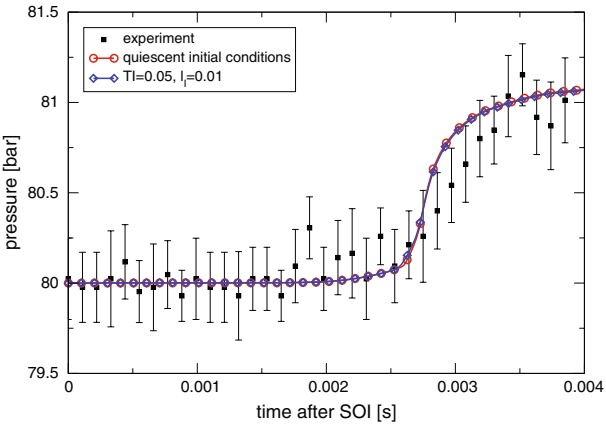


**Fig. 16** Pressure variation with time for different initial background air turbulence levels: quiescent conditions vs. prescribed initial turbulence intensity (TI) of 5% and an initial turbulent length scale ($l_I$) of 10 mm. The Huh spray model [51] and the Liu et al. [59] mechanism have been used; the air temperature is at the nominal 776 K

The sensitivity of the results with respect to the integration method has also been checked. Figure 18 shows a comparison of the integration method from [34, 44] which uses three fractional steps to the formerly employed two-step approach documented

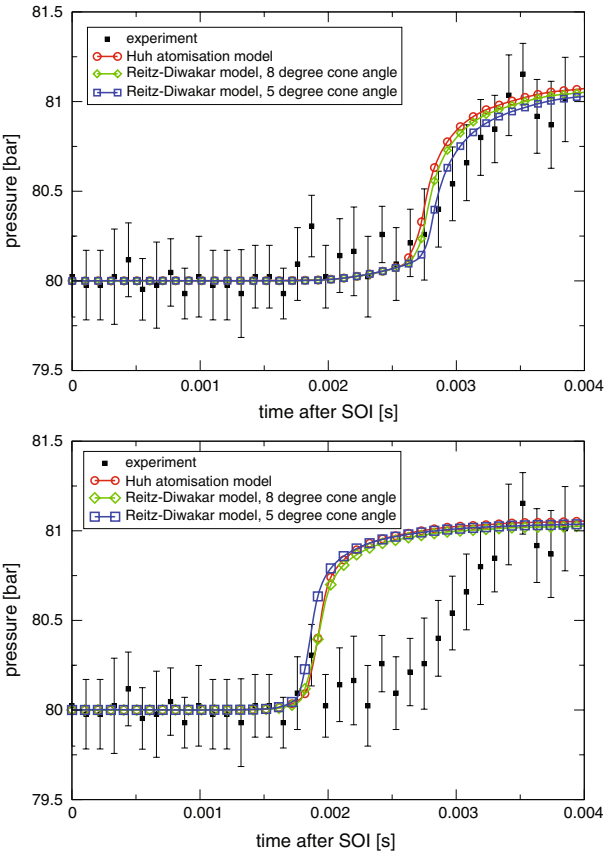


**Fig. 17** Pressure variation with time for Liu et al. mechanism (*upper*, [59]) and Bikas mechanism (*lower*, [58]) using different atomisation models: For the Reitz–Diwakar model [52] the cone angle is prescribed; the Huh model [51] computes it. Air temperature is at the nominal 776 K

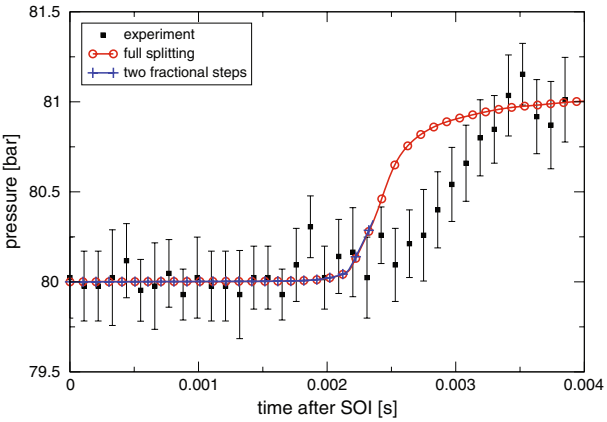


**Fig. 18** Pressure variation with time for two different splitting approaches for the CMC equations. The Huh spray model [51] and the Bikas mechanism [58] have been used, the air temperature is at 765 K

in [33]. When an identical external time step of $1.0 \times 10^{-6}$ s is applied, the fully split solution procedure shows marginally earlier ignition, which gives credence to the methodology and allows for substantial gains concerning the computational costs. The two-step calculation was aborted after roughly one third of the total pressure increase due to an almost identical slope and the high computation costs involved in progressing the solution further.

### *4.2.4 Ignition location*

The comparison of the ignition spot is based on the location of the computed OH mass fractions with the OH* chemiluminescence image data. Two sets of comparisons have been carried out: For the Bikas mechanism the Huh model has been employed and the influence of the air temperature has been assessed. At the lowest temperature of 755 K, the ignition time is comparable to the experiment. As can be seen from Fig. 19, ignition occurs at mixture fractions close to the most reactive and the location is slightly under predicted for the two lowered temperatures. For the Liu et al. mechanism, which showed good agreement for the ignition time, sensitivity with respect to the three different spray models is shown in Fig. 20 at the time of ignition. For the Huh model, the simulation predicts ignition slightly less far downstream than it is seen in the measurement and the Reitz–Diwakar model with 5° substantially over predicts it. With a cone angle of 8° the Reitz–Diwakar shows good agreement. From these findings it can be concluded, that despite only minor influences on the ignition timing and pressure increase as discussed above, the specifics of the atomisation model can have an effect on the ignition location which is comparable to the choice of chemistry and initial temperature.

### *4.2.5 Computational expense*

To assess the computational expense of the methodology, additional calculations have been performed using the 'Laminar and Turbulent Characteristic Time' (LaTCT) eddy break-up model available within STAR-CD using a single step, irreversible chemistry for heptane ($C_7H_{16}+11O_2 \rightarrow 7CO_2+8H_2O$). It was observed (not shown) that (a) the ignition delay predictions obtained therewith—which are treated by the 'Shell model' [67]—are close to the ones from the Bikas chemistry at

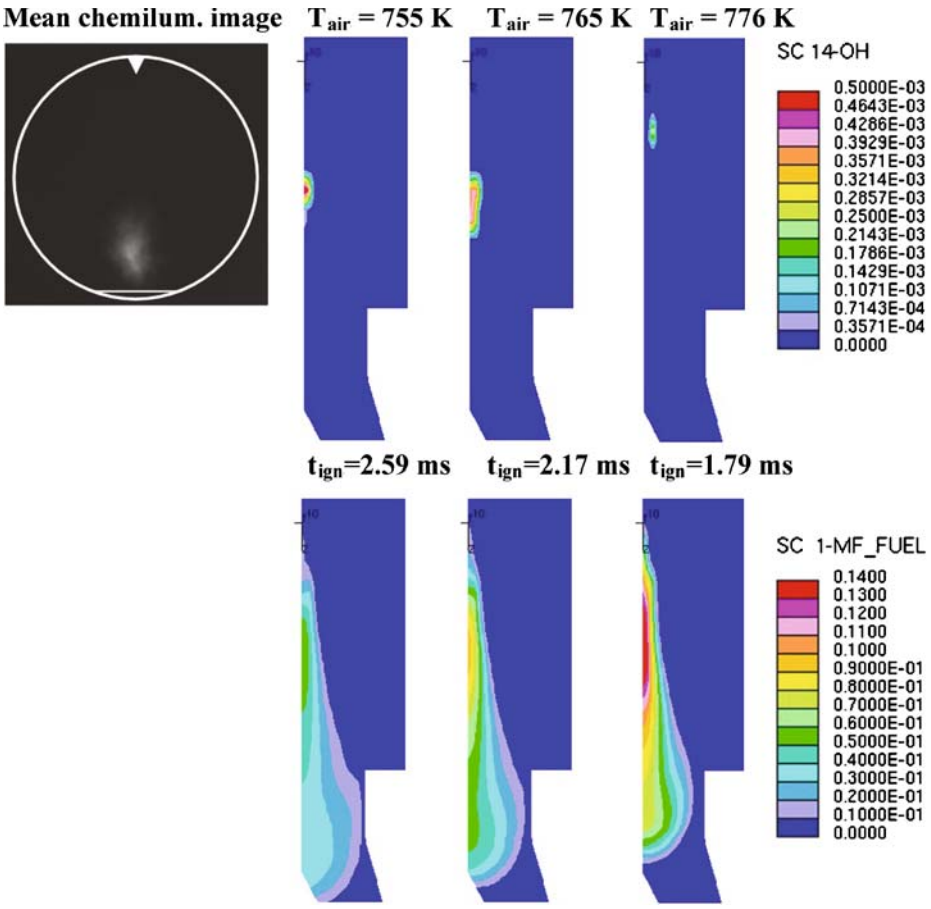


**Fig. 19** Ignition location comparison: mean OH* chemiluminescence signal averaged from 48 individual realisations 2.5 ms after start of injection (*upper left*); the *white circle* symbolises the cell window, the *straight line at the bottom* the location of the wall and the triangle the injector. Simulated OH mass fraction (*upper row*) and mixture fraction (*lower row*) iso-contours at the predicted time of ignition. Initial air temperature set to 755, 765 and 776 K (from *left* to *right*); the Huh spray model [51] and the Bikas mechanism [58] have been used

the nominal temperature and (b) the rate of change of pressure is strongly dependent on the model scaling factor for the turbulent characteristic time.

The LaTCT model requires solution of two additional transport equations in the CFD code, namely the fuel mass fraction and the mixture fraction. All remaining species mass fractions are proportional to the fuel depletion. In contrast, in the CMC code there are 40 radial by 23 axial CMC nodes, multiplied with 101 grid nodes in conserved scalar space, times 22 or 31 species amounting to 2,880,520 or 2,044,240 unknowns depending on the chemistry employed. Due to the splitting methodology discussed above and the stiff solver the large number of unknowns can be treated efficiently. Nonetheless, in terms of computing time, the ratios between the CMC model and the LaTCT model are roughly 80 and 60 for the two chemistries.

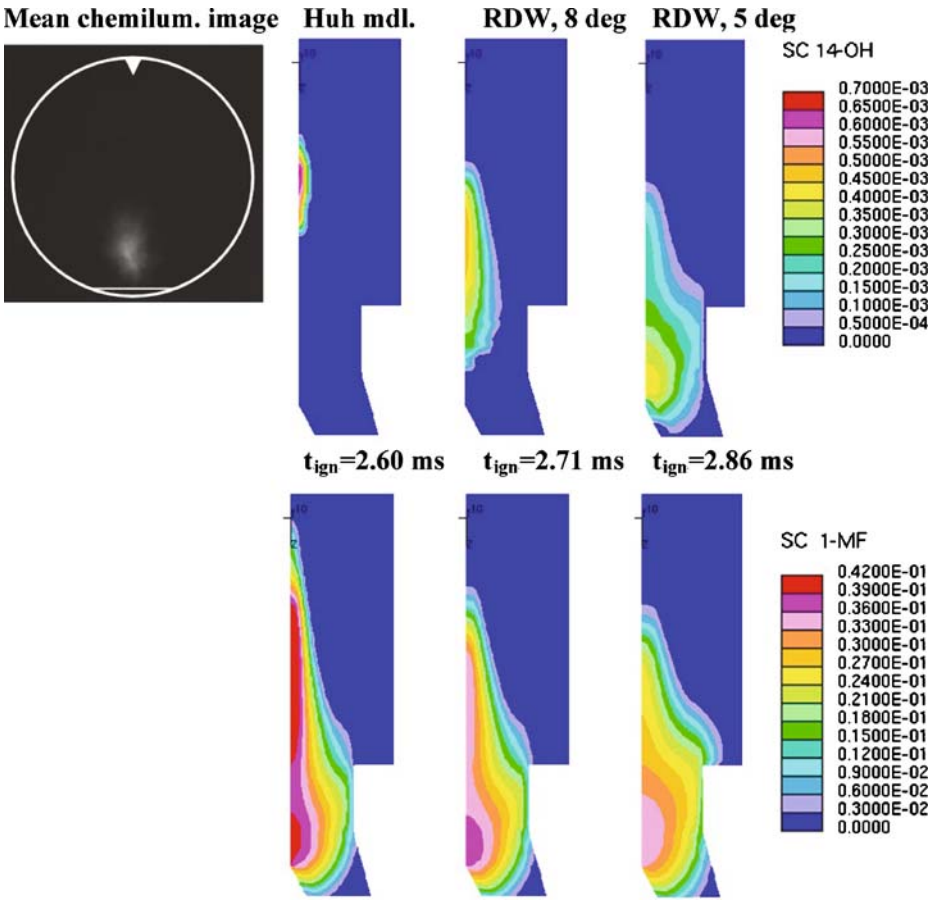


**Fig. 20** Ignition location comparison: mean OH* chemiluminescence signal averaged from 48 individual realisations 2.5 ms after start of injection (*upper left*); the *white circle* symbolises the cell window, the *straight line at the bottom* the location of the wall and the triangle the injector. Simulated OH mass fraction (*upper row*) and mixture fraction (*lower row*) iso-contours at the time of ignition for the Huh model [51], the Reitz–Diwakar Model [52] with 8° and 5° cone angle (from *left* to *right*). The Liu et al. mechanism [59] has been used at the nominal air temperature of 776 K

## 5 Conclusions

A closed high pressure high temperature combustion chamber with optical access has been used to obtain data for auto-igniting *n*-heptane sprays at diesel engine relevant conditions. The pressure signal collected for heat release validation revealed that the ignition delay after start of injection and the subsequent pressure rise were highly reproducible for numerous realisations of the experiment. As ignition delays are highly sensitive to small changes in the initial temperature it can hence be concluded, that the initial conditions in the test rig and the fuel injection are highly repeatable. From the chemiluminescence images it was evident however, that the ignition location showed substantial variability. Schlieren images and Mie scattering

images were recorded in order to provide liquid and gas phase spray data for model calibration purposes.

An elliptic CMC code coupled to a flow field solver has subsequently been applied to investigate this set-up numerically, with the emphasis to identify sensitivities of the simulation results with respect to sub-models, initial conditions and chemical mechanism. The pressure trace has been used to validate the calculated heat release from the combustion; both the rate of increase as well as the total pressure rise are quite well predicted for two chemical mechanisms investigated, despite strong differences in the ignition delays.

As expected, the computed ignition delays showed a very strong sensitivity to the choice of chemical mechanism and the initial flow field temperature. For the conditions investigated, prescribed low levels of turbulence in the background air only lead to minor differences in the ignition delays and pressure development. Uncertainties with respect to the chamber air temperature measurement have been modelled by varying the initially prescribed temperature by 1.5% and 3%. While for this well controlled setup with heated walls these inaccuracies are quantifiable, in engine calculations large uncertainties in temperature and turbulence levels persist when prescribing initial conditions at intake valve closure. The results both in terms of ignition delay and more importantly of ignition location indicate that highly accurate temperature measurements are of similar importance as the choice of mechanism for accurate predictions when using sophisticated combustion models.

Comparisons of the liquid and gas phase spray penetrations by means of Mie scattering and Schlieren imaging techniques revealed that qualitatively reasonable agreement can be achieved using 'standard' models for the spray atomization process. The predictions of the ignition delays and the rate of pressure rise are only slightly affected by the choice of these models and the prescribed cone angle. The ignition location compared by means of the chemiluminescence signal of OH* however shows very strong dependence on the spray atomisation model and prescribed initial cone angle. In cases where the location of the flame is important, e.g. in case of engine combustion with substantial heat losses due to 'cold' walls, these finding indicate that spray atomization plays a major role and could have a similar influence on the heat release rate prediction as the choice of the chemical mechanism.

These findings suggest that further progress in the field of two-phase flow modelling is required, both for CFD and CMC solvers. Diesel engine simulation would also benefit greatly from advances in the development of reduced chemistries suitable for auto-ignition at diesel engine pressures and from time-resolved velocity field measurements allowing in particular for derivation of initial turbulence quantities as well as from improved, high accuracy temperature measurement techniques.

**Acknowledgements** This project was supported by the Swiss Federal Office of Energy (BfE grant nos. 47495 and 102688) and the Swiss Competence Center Energy and Mobility (CCEM-CELaDE). The authors thank Peter Schroll, University of Cambridge, for the helpful discussions concerning CMC two-phase related modelling and implementation.

## References

1. Baritaud, T.A., Heinze, T.A., Le Coz, J.F.: Spray and self-ignition visualization in a DI diesel engine. SAE 940681 (1994)
2. Bruneaux, G., Verhoeven, D., Baritaud, T.: High pressure diesel spray and combustion visualization in a transparent model diesel engine. SAE 1999-01-3648 (1999)

3. Desantes, J.M., Pastor, J.V., Payri, R., Pastor, J.M.: Experimental characterization of internal nozzle flow and diesel spray behaviour. Part II: evaporative conditions. At. Sprays **15**, 517–543 (2005). doi:10.1615/AtomizSpr.v15.i5.30
4. Dec, J.E., Espey, C.: Chemiluminescence imaging of autoignition in a DI diesel engine. SAE 982685 (1998)
5. Koss, H.J., Brüggemann, D., Wiartalla, A., Bäcker, H., Breuer, A.: Investigations of the influence of turbulence and type of fuel on the evaporation and mixture formation in fuel sprays. Final Report of JOULE Project on Integrated Diesel European Action (IDEA) (1992)
6. Vogel, S., Hasse, C., Gronki, J., Andersson, S., Peters, N., Wolfrum, J., Schulz, C.: Numerical simulation and laser-based imaging of mixture formation, ignition, and soot formation in a diesel spray. Proc. Combust. Inst. **30**, 2029–2036 (2005). doi:10.1016/j.proci.2004.08.202
7. Liao, C., Terao, K.: A statistical investigation of ignition in a fuel spray using a shock tube. JSME Int. J. Ser. B **38**, 136–142 (1995)
8. Kosaka, H., Drewes, V.H., Catalfamo, L., Aradi, A.A., Iida, N., Kamimoto, T.: Two-dimensional imaging of formaldehyde formed during the ignition process of a diesel fuel spray. SAE 2000-01-0236 (2000)
9. Akiyama, H., Nishimura, H., Yasumitsu, I., Iida, N.: Study of diesel combustion and ignition using high-pressure fuel injection and a micro-hole nozzle with a rapid compression machine: improvement of combustion using low cetane number fuel. JSAE Rev. **19**, 319–327 (1999). doi:10.1016/S0389-4304(98)00024-1
10. Balles, A., Heywood, J.B.: Fuel-air mixing and diesel combustion in a rapid compression machine. SAE 880206 (1988)
11. Pikett, L.M., Siebers, D.L.: Soot in diesel fuel jets: effects of ambient temperature, ambient density, and injection pressure. Combust. Flame **138**, 114–135 (2004). doi:10.1016/j.combustflame.2004.04.006
12. Margari, O.-N.: Optical investigation of soot evolution in spray combustion—influence of fuel composition and injection parameters. Ph.D. Thesis, ETH Zürich, Switzerland, Diss. ETH Nr. 17143 (2007)
13. Bruneaux, G.: Liquid and vapour spray structure in high-pressure common rail diesel injection. At. Sprays **11**, 533–556 (2001)
14. Kong, S.-C., Han, Z., Reitz, D.: The development and application of a diesel ignition and combustion model for multidimensional engine simulation. SAE950278 (1995)
15. Hasse, C., Peters, N.: A two mixture fraction flamelet model applied to split injections in a DI diesel engine. Proc. Combust. Inst. **30**, 2755–2762 (2005). doi:10.1016/j.proci.2004.08.166
16. Barths, H., Hasse, C., Bikas, G., Peters, N.: Simulation of combustion in direct injection diesel engines using Eulerian particle flamelet model. Proc. Combust. Inst. **28**, 1161–1168 (2000). doi:10.1016/S0082-0784(00)80326-4
17. Hollmann, C., Gutheil, E.: Modelling of turbulent spray diffusion flames including detailed chemistry. Proc. Combust. Inst. **26**, 1731–1738 (1996)
18. Tap, F.A., Veynante, D.: Simulation of lif-off on a Diesel jet using a generalized flame surface density modelling approach. Proc. Combust. Inst. **30**, 919–926 (2005). doi:10.1016/j.proci.2004.08.170
19. Zhang, Y.Z., Kung, E.H., Haworth, D.C.: A PDF method for multidimensional modelling of HCCI engine combustion: effects of turbulence/chemistry interactions on ignition timing and emissions. Proc. Combust. Inst. **30**, 2763–2771 (2005). doi:10.1016/j.proci.2004.08.236
20. Lehtiniemi, H., Mauss, F., Bathasar, M., Magnusson, I.: Modelling diesel spray autoignition using detailed chemistry with a progress variable approach. Combust. Sci. Technol. **178**, 1977–1997 (2006). doi:10.1080/00102200600793148
21. Michel, J.-B., Colin, O., Veynante, D.: Modeling ignition and chemical structure of partially premixed turbulent flames using tabulated chemistry. Combust. Flame **152**, 80–99 (2008). doi:10.1016/j.combustflame.2007.09.001
22. Roomina, M.R., Bilger, R.W.: Conditional moment closure (CMC) predictions of a turbulent methane-air jet flame. Combust. Flame **125**, 1176–1195 (2001). doi:10.1016/S0010-2180(01)00237-1
23. Devaud, C.B., Bray, K.N.C.: Assessment of the applicability of conditional moment closure to a lifted turbulent flame: first order model. Combust. Flame **132**, 102–114 (2003). doi:10.1016/S0010-2180(02)00427-3
24. Kim, I.S., Mastorakos, E.: Simulations of turbulent lifted jet flames with two-dimensional conditional moment closure. Proc. Combust. Inst. **30**, 911–918 (2004). doi:10.1016/j.proci.2004.08.039

25. Fairweather, M., Woolley, R.M.: First-order conditional moment closure modeling of turbulent, non-premixed methane flames. Combust. Flame **138**, 3–19 (2004). doi:10.1016/j.combustflame.2004.03.001
26. Kim, I.S., Mastorakos, E.: Simulations of turbulent non-premixed counterflow flames with first-order conditional moment closure. Flow Turbul. Combust. **76**, 133–162 (2006). doi:10.1007/s10494-006-9009-7
27. Navarro-Martinez, S., Kronenburg, A.: LES-CMC simulations of a turbulent bluff-body flame. Proc. Combust. Inst. **31**, 1721–1728 (2007). doi:10.1016/j.proci.2006.07.212
28. Fairweather, M., Woolley, R.M.: Conditional moment closure calculations of a swirl-stabilized, turbulent non-premixed methane flame. Combust. Flame **151**, 397–411 (2007). doi:10.1016/j.combustflame.2007.07.009
29. Kim, S.H., Huh, K.Y., Fraser, A.R.: Modeling autoignition in turbulent methane jet by the conditional moment closure method. Proc. Combust. Inst. **28**, 185–191 (2000)
30. De Paola, G., Kim, I.S., Mastorakos, E.: Second-order conditional moment closure simulations of autoignition of a n-heptane plume in a turbulent coflow of heated air. Flow Turbul. Combust. **82**, 455–475 (2009). doi:10.1007/s10494-008-9183-x
31. El Sayed, A., Milford, A., Devaud, C.B.: Modelling of autoignition for methane-based fuel blends using conditional moment closure. Proc. Combust. Inst. **32**, 1621–1628 (2009). doi:10.1016/j.proci.2008.06.032
32. Kim, W.T., Huh, K.Y.: Numerical simulation of spray autoignition by the first-order conditional moment closure model. Proc. Combust. Inst. **29**, 569–576 (2002). doi:10.1016/S1540-7489(02)80073-6
33. Wright, Y.M., De Paola, G., Boulouchos, K., Mastorakos, E.: Simulations of spray auto-ignition and flame establishment with two-dimensional CMC. Combust. Flame **143**, 402–419 (2005). doi:10.1016/j.combustflame.2005.08.022
34. De Paola, G., Mastorakos, E., Wright, Y.M., Boulouchos, K.: Diesel engine simulations with multi-dimensional conditional moment closure. Combust. Sci. Technol. **180**, 883–899 (2008). doi:10.1080/00102200801894273
35. Bertola, A.G.: Technologies for Lowest NOx and particulate emissions in DI-diesel engine combustion—influence of injection parameters, EGR and fuel composition. Ph.D. Thesis, ETH Zürich, Switzerland, Diss. ETH No. 15373 (2003)
36. Schneider, B.M.: Experimentelle Untersuchungen zur Spraystruktur in transienten, verdampfenden und nicht verdampfenden Brennstoffstrahlen unter Hochdruck. Ph.D. Thesis, ETH Zürich, Switzerland, Diss. ETH No. 15004 (2003)
37. Settles, G.S.: Schlieren and Shadowgraph Techniques: Visualizing Phenomena in Transparent Media. Springer, New York (2001)
38. "Ansprechzeiten von Thermocoax Thermoelementen", Philips I+F/Industrial OEM product documentation 9498 02 3 211 18 EWI 8707
39. STAR-CD v3.26 © cd-adapco (2006)
40. Klimenko, A.Y.: Multicomponent diffusion of various admixtures in turbulent flow. Fluid Dyn. **25**, 327–334 (1990)
41. Bilger, R.W.: Conditional moment closure for turbulent reacting flows. Phys. Fluids A **5**, 436–444 (1993). doi:10.1063/1.858867
42. Klimenko, A.Y., Bilger, R.W.: Conditional moment closure for turbulent combustion. Progr. Energ. Combust. Sci. **25**, 595–687 (1999). doi:10.1016/S0360-1285(99)00006-4
43. Hergart, C., Peters, N.: Applying the representative interactive flamelet model to evaluate the potential effect of wall heat transfer on soot emissions in a small-bore direct-injection diesel engine. J. Eng. Gas Turbine Power **124**, 1042–1052 (2002). doi:10.1115/1.1473147
44. De Paola, G.: Conditional moment closure for autoignition in turbulent flows. Ph.D. Thesis, University of Cambridge, UK (2007)
45. Mastorakos, E.: Ignition of turbulent non-premixed flames. Progr. Energ. Combust. Sci. **35**, 57–97 (2009). doi:10.1016/j.pecs.2008.07.002
46. Colin, O., Benkenida, A.: A new scalar fluctuation model to predict mixing in evaporating two-phase flows. Combust. Flame **134**, 207–227 (2003). doi:10.1016/S0010-2180(03)00096-8
47. Réveillon, J., Vervisch, L.: Spray vaporization in nonpremixed turbulent combustion modelling: a single droplet model. Combust. Flame **121**, 75–90 (2000). doi:10.1016/S0010-2180(99)00157-1
48. Demoulin, F.X., Borghi, R.: Assumed PDF modeling of turbulent spray combustion. Combust. Sci. Technol. **158**, 249–271 (2000). doi:10.1080/00102200008947336
49. Rogerson, J.W., Kent, J.H., Bilger, R.W.: Conditional moment closure in a baggasse-fired boiler. Proc. Combust. Inst. **31**, 2805–2811 (2007). doi:10.1016/j.proci.2006.07.112

50. Mortensen, M., Bilger, R.W.: Derivation of the conditional moment closure equations for spray combustion. Combust. Flame **156**, 62–72 (2009). doi:10.1016/j.combustflame.2008.07.007
51. Huh, K.Y., Gosman, A.D.: A phenomenological model of diesel spray atomization. In: Proc. Int. Conf. on Multiphase Flows, Tsukuba, Japan (1991)
52. Reitz, R.D., Diwakar. R.: Effect of drop breakup on fuel sprays. SAE 860469 (1986)
53. Bai, C., Gosman, A.D.: Development of methodology for spray impingement simulation. SAE 950283 (1995)
54. Kim, I.S.: Conditional moment closure for non-premixed turbulent combustion. Ph.D. Thesis, University of Cambridge, UK (2004)
55. Mastorakos, E., Baritaud, T.A., Poinsot, T.J.: Numerical simulation of autoignition in turbulent mixing flows. Combust. Flame **109**, 198–223 (1997). doi:10.1016/S0010-2180(96)00149-6
56. Curran, H.J., Gaffuri, P., Pitz, W.J., Westbrook, C.K.: A comprehensive modeling study of n-heptane oxidation. Combust. Flame **114**, 149–177 (1998). doi:10.1016/S0010-2180(97)00282-4
57. Hewson, J.C.: Pollutant emissions from nonpremixed hydrocarbon flames. Ph.D. Thesis, University of California, San Diego, USA (1997)
58. Bikas, G.: Kinetic mechanisms for hydrocarbon ignition. Ph.D. Thesis, University of Aachen, Germany (2001)
59. Liu, S., Hewson, J.C., Chen, J.H., Pitsch, H.: Effect of strain rate on high-pressure nonpremixed n-heptane autoignition in counterflow. Combust. Flame **137**, 320–339 (2004). doi:10.1016/j.combustflame.2004.01.011
60. Ciezky, H.K., Adomeit, G.: Shock-tube investigation of self-ignition of n-heptane–air mixtures under engine relevant conditions. Combust. Flame **93**, 421–433 (1993). doi:10.1016/0010-2180(93)90142-P
61. Fast, G., Kuhn, D., Class, A.G., Maas, U.: Auto-ignition during instationary jet evolution of dimethyl ether (DME) in a high-pressure atmosphere. Combust. Flame **156**, 200–213 (2009). doi:10.1016/j.combustflame.2008.07.015
62. Bruneaux, G.: Mixing process in high pressure diesel jets by normalized laser induced exciplex fluorescence part I: free jet. SAE 2005-01-2100 (2005)
63. Boulouchos, K., Margari, O.-N., Escher, A., Barroso, G., Schneider, B., Kunte, S.: Optical diagnostic on diesel sprays for the validation of computer aided simulation. In: 6. Internationales Symposium für Verbrennungsdiagnostik, Baden-Baden (2003)
64. Hilbert, R., Thévenin, D.: Autoignition of turbulent non-premixed flames investigated using direct numerical simulation. Combust. Flame **128**, 22–37 (2002). doi:10.1016/S0010-2180(01)00330-3
65. Pizza, G., Wright, Y.M., Weisser, G., Boulouchos, K.: Evaporating and non-evaporating diesel spray simulation: comparison between the ETAB and wave break-up model. Int. J. Veh. Des. **45**, 80–99 (2007). doi:10.1504/IJVD.2007.013672
66. Barroso, G., Schneider, B., Boulouchos, K.: An extensive parametric study on diesel spray simulation and verification with experimental data. SAE2003-01-3230 (2003)
67. Halstead, M.P., Kirsch, L.J., Quinn, C.P.: The autoignition of hydrocarbon fuels at high temperatures and pressures—fitting of a mathematical model. Combust. Flame **30**, 45–60 (1977). doi:10.1016/0010-2180(77)90050-5